



Two-dimensional dual carbon-coupled defective nickel quantum dots towards highly efficient overall water splitting



Ziliang Chen^{a,1}, Hongbin Xu^{a,1}, Yuan Ha^a, Xuanyi Li^{b,c}, Miao Liu^{b,c,d}, Renbing Wu^{a,*}

^a Department of Materials Science, Fudan University, Shanghai, 200433, PR China

^b Institute of Physics, Chinese Academy of Sciences, Beijing, 100190, PR China

^c Center of Materials Science and Optoelectronics Engineering, University of Chinese Academy of Sciences, Beijing, 100049, PR China

^d Songshan Lake Materials Laboratory, Dongguan, Guangdong, 523808, PR China

ARTICLE INFO

Keywords:

Ni quantum dots
2D zeolitic imidazolate framework
Oxygen evolution reaction
Hydrogen evolution reaction
Water splitting

ABSTRACT

Rational design of highly efficient and cost-effective bifunctional electrocatalyst for both oxygen evolution reaction (OER) and hydrogen evolution reaction (HER) is extremely desirable but still challenging for electrochemical water splitting. Herein, we report the synthesis of hybrid composites consisting of defective nickel quantum dots (Ni QD) encapsulated in N-doped carbon (NC) anchored on the surface of reduced graphene oxide (Ni QD@NC@rGO) through a low-temperature pyrolysis of rGO-wrapped two dimensional (2D) sheet-like nickel zeolite imidazolate framework. The as-fabricated Ni QD@NC@rGO catalysts only require overpotentials of 265 and 133 mV to deliver a current density of 10 mA cm⁻² for OER and HER in 1.0 M KOH, respectively. Remarkably, an alkaline electrolyzer constructed with Ni QD@NC@rGO catalyst for both anode and cathode can drive a current density of 10 mA cm⁻² at a low cell voltage of 1.563 V, superior to that of the Pt@C||IrO₂@C couple (1.614 V). The enhanced electrocatalytic performance of Ni QD@NC@rGO can be mainly attributed to its 2D hierarchically porous structure and the synergistic effect of the highly dispersed Ni QD, *in-situ* coupled thin-layer NC and rGO, giving rise to a large surface active sites exposure, enhanced electron/ion transfer ability and optimal Gibbs free energy of adsorption.

1. Introduction

Hydrogen has been regarded as one of the most ideal energy carriers for the future owing to its high gravimetric energy, clean exhaust products, and renewable nature [1–6]. As one route for the generation of hydrogen, electrochemical water splitting has sparked great attention as it not only can convert electric energy into chemical energy in a green manner, but also can be easily integrated with other intermittent energy sources (e.g., solar and wind) [7–9]. However, a high driving overpotential is required in the practical electrolysis process due to the activation energy barriers of two core half-reactions involved in water splitting, *i.e.*, oxygen evolution reaction (OER) and hydrogen evolution reaction (HER) [10–12]. To reduce overpotentials, precious Ir/Ru-based and Pt-based materials have been developed as effective electrocatalysts for OER and HER processes, respectively [13,14]. Unfortunately, the large-scale utilization of these noble metals has been severely hampered by their high cost and limited supply on the earth.

Over the past decades, in order to explore an alternative to precious-

metal catalysts, various none-precious 3d transition metals (TMs) (e.g., Fe, Co, Ni, etc.) and their derivatives have been intensively investigated [15–28]. Among them, TMs nanoparticles encapsulated into the nitrogen-doped carbon (TMs@NC) are of particular interest as an unique category of heterogeneous catalysts for HER or OER [29–32]. Within this structure, the coupled carbon shells not only mitigate the TMs cores from strong acid/alkaline corrosions, but also capture the electrons from TMs nanoparticles and accelerate their transport. In addition, the doped nitrogen species can tailor the charge distribution and electron spin density of carbon, further promoting the catalytic reaction. Nevertheless, developing a convenient and reliable synthesis method for highly dispersed TMs encapsulated within NC still remains challenging.

Metal-organic frameworks (MOFs), a class of crystalline porous materials consisting of metal ions coordinated organic linkers, have been demonstrated to be a suitable precursor to construct TM@NC-based composites by pyrolysis [33–50]. For instance, Su et al. reported that the encapsulation of Co nanoparticles in the porous N-doped

* Corresponding author.

E-mail address: rbwu@fudan.edu.cn (R. Wu).

¹ Z. Chen and H. Xu contributed equally to this work.

carbon nanotubs (CNTs) could be realized by pyrolyzing the (Zn, Co) bimetallic zeolitic imidazolite framework (ZIF) at 900 °C, which could achieve a current density of 10 mA cm⁻² at an overpotential of 370 mV for OER in 1.0 M KOH [48]. Zheng et al. synthesized CuCo@NC composite catalyst by annealing the Cu-doped Co-MOF at 800 °C and found that it could afford 10 mA cm⁻² at an overpotential of 145 mV in 0.5 M H₂SO₄ for HER [49]. More recently, Zhao et al. prepared hybrid Fe-Ni@NC-CNTs composite catalyst by decomposing MIL-88-Fe/Ni-dicyandiamide at 800 °C, showing OER and HER activity with an overpotential of 274 and 202 mV, respectively, at 10 mA cm⁻² in 1.0 M KOH [50]. Although this MOFs-driven process allows easy access to TMs@NC composites, a high pyrolysis temperature over 700 °C was usually required, which may add an extra energy consumer and block the practical application. Additionally, these MOF-derived TMs@NC catalysts pyrolyzed at high temperatures usually exhibited an undesired aggregation of TMs nanoparticles with nonuniform distribution and low specific surface area, which are unbenevolent to the utilization and exposure of catalytic active sites, thus leading to the limited OER and/or HER activity. In this context, to further improve the catalytic activity, exploring novel MOF precursors to achieve TMs@NC with homogeneously distributed active sites, favorable specific surface area and strong electron penetration capability at low temperature is highly desirable.

On the other hand, previous studies indicated that TMs-based catalyst in the form of two-dimensional (2D) morphology could significantly increase the accessible surface areas and active edges compared with their 3D counterparts, which is believed to be exposing more active sites and enhancing their electrocatalytic activity [51]. Nevertheless, even with MOF-driven strategies, there has been rarely success in synthesizing TMs@NC with well-defined 2D geometry possibly due to difficulties in lacking of appropriate 2D MOF precursor.

Motivated by above issues, herein, for the first time, we have developed a novel 2D sheet-like hybrid composites consisting of defective Ni quantum dots (Ni QDs) encapsulated in thin-layer N-doped carbon (NC) grafted on reduced graphene oxide (rGO) (Ni QD@NC@rGO) by a low-temperature pyrolysis of rGO-coated 2D Ni-zeolitic imidazolate framework (Ni-ZIF@rGO). This strategy integrates the merits of both 2D Ni-ZIF and 2D graphene. Specifically, the ultrathin feature and low thermal stability of 2D Ni-ZIF provides abundant coordinated unsaturated metal sites for the formation of defective Ni clusters coupled with N-C during low-temperature pyrolysis and ensures products richly exposed catalytic active sites [52–55]. On the other hand, the wrapped graphene not only greatly enhances the electrical conductivity and mechanical flexibility of the composite, but also inhibits the possible aggregation of Ni nanoparticles caused by the easy self-stacking of 2D ZIFs. Thus, as expected, such low-temperature-fabricated 2D Ni QD@NC@rGO composites exhibited ultralow overpotentials of 265 and 133 mV at a current density of 10 mA cm⁻² for OER and HER, respectively, and robust durability in the alkaline solution. Moreover, the Ni QD@NC@rGO composites used as bifunctional electrocatalyst for overall-water-splitting can achieve 10 mA cm⁻² at a cell voltage of only 1.563 V, superior to those of most previously reported TMs-carbon-based catalysts and even better than that of the IrO₂@C||Pt@C counterpart. More encouraging, the developed strategy is universal and controllable, which can be easily extended to synthesize other 2D binary TM QD@NC@rGO composites.

2. Experimental section

2.1. Preparation of graphene oxide (GO)

On the basis of the modified Hummers' method, GO was prepared via the oxidation of natural graphite powder followed by the purification [56].

2.2. Preparation of 2D Ni-ZIF@rGO and 2D Ni-Co-ZIF@rGO

In a typical synthesis of 2D Ni-ZIF@rGO, 5 mL of methanol solution containing 290 mg of Ni(NO₃)₂·6H₂O were firstly mixed with 17 mL of 4 mg mL⁻¹ graphene oxide aqueous suspension under 20 min of stirring. Then, 5 mL of methanol solution containing 328 mg of 2-Methylimidazole (2-MeIm) was slowly added into above solution. The mixture was stirred at room temperature for 10 min and then transferred into an autoclave (50 mL) and kept at 180 °C for 6 h. After cooling to room temperature, the 2D Ni-ZIF@rGO with sandwich-like structure was obtained by centrifugation at 8000 rpm for 5 min, washed four times with deionized water, and dried in a freeze dryer with a vacuum at –50 °C for 48 h. The fabrication procedure of 2D Ni-Co-ZIF@rGO is similar to that making 2D Ni-ZIF@rGO composites but using mixture of Ni(NO₃)₂·6H₂O (260 mg) and Co(NO₃)₂·6H₂O (30 mg) instead of Ni(NO₃)₂·6H₂O.

2.3. Preparation of Ni QD@NC@rGO and Ni-Co QD@NC@rGO

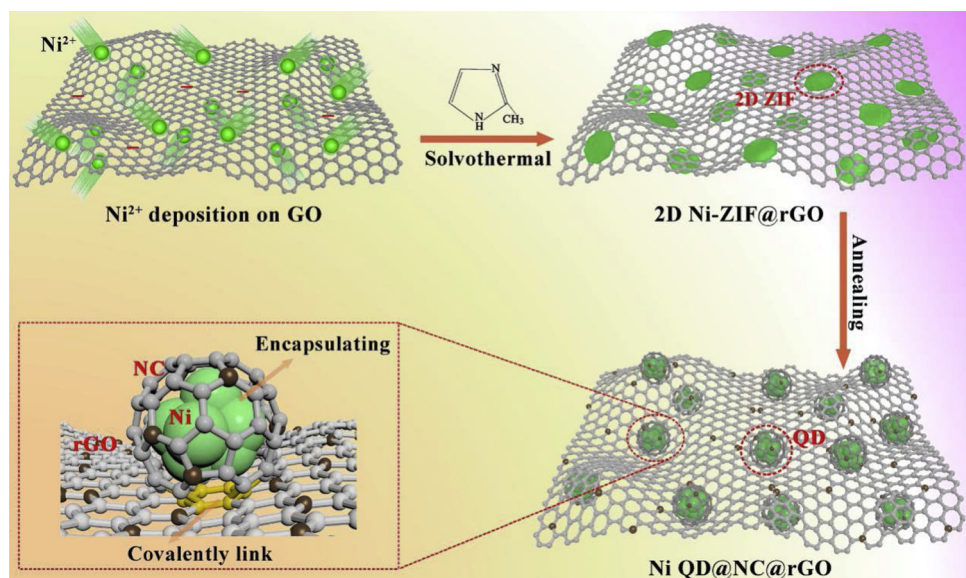
The Ni QD@NC@rGO composite was synthesized by one-pot thermal treatment. Typically, a combustion boat loaded with 2D Ni-ZIF@rGO precursor was put into a tube furnace and then heated to 450 °C at the rate of 2 °C min⁻¹ and maintained at this temperature for 2 h under a flow Ar gas. For comparison, the 2D Ni-ZIF@rGO precursors were annealed at 350 and 550 °C for 2 h under a flow Ar gas, respectively, and the obtained products are denoted as A-Ni-ZIF@rGO-350 and A-Ni-ZIF@rGO-550, respectively. On the other hand, the bare graphene after solvothermal reaction was also annealed at 450 °C for 2 h under a flow Ar gas, and the obtained products are denoted as A-rGO-450. The Ni-Co@NC@rGO composites were prepared by one-pot annealing 2D Ni-Co-ZIF@rGO precursors at 450 °C for 2 h under a flow Ar gas.

2.4. Materials characterizations

To identify the phase composition of the as-prepared composites, powder X-ray diffraction (XRD) was conducted by using a D8 ADVANCE X-ray diffractometer with Cu K_α radiation ($\lambda = 1.5406 \text{ \AA}$). To further evaluate the phase structures, the obtained XRD patterns were analyzed by using the RIETAN-2000 program based on the Rietveld method [57]. The detail information regarding with the element chemical states, morphology, and microstructure of the as-prepared composites were obtained by the characterizations of X-ray energy disperse spectrometry (XPS, XSAM-800 spectrometer with an Mg K_α radiation source), field-emission scanning electron microscope (FESEM, ZEIS, Ultra-55), and transmission electron microscope (TEM, JEOL JEM-2100 F), respectively. High-resolution XPS were taken with a monochromatic Al K_{α1} x-ray on a SPECS PHOIBOS 150 electron energy analyzer. Raman spectroscopy was recorded on an Invia/Reflrx Laser Micro-Raman spectroscope (Horiba Jobin Yvon, French) to characterize the carbon structure. Room-temperature electron paramagnetic resonance (EPR) spectra were carried out on a Bruke EMPplus EPR spectrometer (300 K, X band). The equipped excitation laser beam wavelength is 532 nm. An Autosorb IQ Gas Sorption System at 77 K was employed to characterize the surface area and pore size volume of the catalysts. Thermogravimetric analysis (TGA) measurements were performed under air/nitrogen atmosphere from room temperature to aimed temperature at a rate of 5 °C min⁻¹ by using America TA-Q500 apparatus. The inductively coupled plasma optical emission spectrometry (ICP, Perkin-Elmer Optima 5300) was used to acquire the chemical composition of the catalysts.

2.5. Electrochemical measurements

The preparation procedures of working electrodes was described as follows. Firstly, 5 mg of as-synthesized catalyst was transferred to a



Scheme 1. Schematic illustration for the synthesis of Ni QD@NC@rGO composites.

mixture solution containing 970 μ L of ethanol and 30 μ L of Dupont Nafion 117 solution (10 wt.%), followed by ultrasonically mixing for 30~50 min to get a homogeneous suspension. Then, dropwise added 10 μ L of above suspension onto the surface of glass carbon (GC) electrode using a microsyringe. Finally, the electrode was allowed to be naturally dried at room temperature.

All electrochemical measurements were performed with computer-controlled workstation (AutoLab PGSTAT302N) in a three-electrode cell at 25 °C. A saturated calomel electrode (SCE) and a carbon rod were employed as the reference electrode and the counter electrode, respectively. Before the linear sweep voltammetry (LSV) tests for OER and HER at a scan rate of 5 mV s⁻¹, the electrode was subjected to continuous cyclic voltammetry cycles with a scan rate of 20 mV s⁻¹ to achieve stable curves. All potentials were calibrated with respect to reversible hydrogen electrode (RHE) based on the equation $E_{\text{vs.RHE}} = E_{\text{vs.SCE}} + 0.2412 + 0.05916 \text{ pH} - iR_s$, where R_s is the resistance of solution. On the basis of the LSV, Tafel slope was obtained. Cyclic voltammetry (CV) was conducted at non-Faradaic region to evaluate the apparent electrochemical double layer capacitance (C_{dl}). Electrochemical Impedance Spectroscopy (EIS) were recorded in a frequency range of 100 kHz – 0.01 Hz at the overpotential of 0.15 V vs. RHE and further analyzed by the Zsimpwin software. The cycle durability of OER and HER activity was implemented by the chronamperometric response in the O₂-saturated and H₂-saturated 1.0 M KOH solution, respectively. Overall water electrolysis was performed in a single-compartment cell, in which modified carbon fiber electrodes (0.5 cm × 0.4 cm) with a catalyst loading of 1.0 mg cm⁻² were used as both the cathode and the anode. To fabricate the electrodes, 40 μ L of the catalyst suspension mentioned above was dripped onto the carbon fiber in total. The electrodes were then dried at 45 °C under vacuum for 2 h. LSV curve of water electrolysis was recorded from 1.0–2.0 V at a scan rate of 5 mV s⁻¹ in 1 M KOH solution. The Faradic efficiency (FE) of the as-fabricated electrodes was determined by the water drainage method. Bulk electrolysis was carried out by biasing the electrodes at a fixed potential. The evolved gas is directly collected and the corresponding gas volume is achieved by displacement of the water column. Ideal gas approximation was employed to determine the moles of gas evolved at different time intervals. FE was finally estimated by comparing the amount of experimentally quantified gas and that of theoretically calculated gas.

2.6. Density functional theory (DFT) calculations

We used the Vienna ab initio software package (VASP) [58] with the projector augmented wave method [59] to perform the first-principle calculations. During the calculation, the generalized gradient approximation (GGA) [60] within the Perdew–Burke–Ernzerhof (PBE) [61] parameterization was employed as the electron exchange–correlation function, and the atomic positions, cell shape as well as cell volume were fully optimized until remaining forces less than 0.01 eV Å⁻¹. Noted that all related magnetic ions are initialized ferromagnetically. The model of Ni encapsulated in N-doped carbon was constructed by using a slab model to mimic the surface and interface of the Ni@C–N system. The Ni (0001) facet was chosen as the terminating surface of the slab as (0001) is the most thermodynamically stable/mostly exposed facet for hcp Ni metal. The Ni (0001) surface was enclosed by a monolayer of carbon and then they were relaxed to reach the ground state of the Ni@C configuration. Because the large enough super cell can represent the reality and keep the H or N atom far from its image atoms for periodical boundary conditioned calculations, allowing us to model the low enough N concentration, a 4 × 4 surface is adopted to achieve the accurate H⁺ absorption energy for H absorption with or without N dopant. The model was involved with ~100 atoms in total, and the calculation used a 1 × 1 × 1 grid mesh for K-space sampling. The N doping was simulated by replacing C with N atom at the concentration of 1/32 and 1/16, which are ~3% and ~6% of the N doping, respectively (named Ni@N₁C₃₁ and Ni@N₂C₃₀, respectively). The model of Ni metal with vanancies was constructed by removing ~10% Ni atoms in the Ni@N₂C₃₀ model (Ni₁@N₂C₃₀). The free energies of the intermediates H^{*} were calculated based on the equation that $\Delta G = \Delta E(\text{H}^*) + \Delta ZPE - T\Delta S$, where $\Delta E(\text{H}^*)$, ΔZPE and ΔS are the binding energy of H species, the zero point energy change, and entropy change of adsorption H, respectively. The contribution of entropies and ZPE for ΔG were used as the previous work [62], in which finally $\Delta G = \Delta E(\text{H}^*) + 0.37 \text{ eV}$. The charge transfer was acquired by subtracting the charge density of charge density of the isolated C (or N–C) and isolated Ni slab from the charge density of the Ni@C (or N–C).

3. Results and discussions

The synthetic route for 2D Ni QD@NC@rGO composites is displayed in **Scheme 1**. Firstly, the carboxylic groups of graphene oxide (GO) captured the Ni²⁺ ions with positive charge through the electrostatic

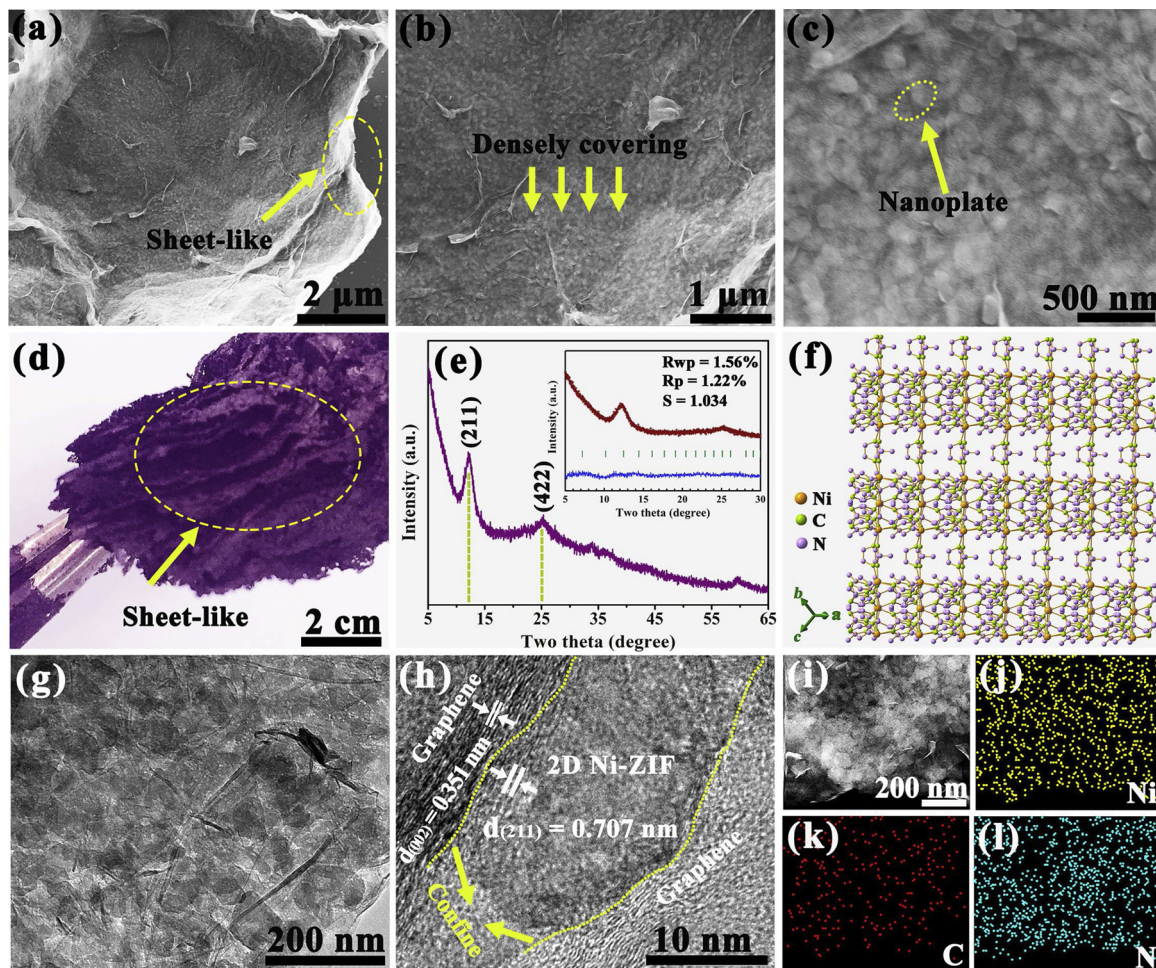


Fig. 1. (a–c) FESEM images, (d) digital image and (e) XRD pattern of 2D Ni-ZIF@rGO composites; (f) illustration of crystal structure of 2D Ni-ZIF; (g) TEM and (h) HRTEM images of 2D Ni-ZIF@rGO composites and the corresponding (i) HAADF-STEM image and corresponding (j) Ni, (k) C, and (l) N elemental mappings. Inset in Fig. 1e: Rietveld refinement of the XRD pattern of 2D Ni-ZIF@rGO composites.

adherence. By further introducing 2-Methylimidazole (2-MeIm) into above solution, a coordination reaction occurs between 2-MeIm and Ni^{2+} , resulting in the *in-situ* nucleation of Ni-ZIF on the surface of GO sheet. Following that, a solvothermal reaction at 180 °C is carried out to allow for achieving the precursor constructed by ultrathin 2D Ni-ZIF nanoplates uniformly and parallel spread on surface of reduced graphene oxide sheet, *i.e.*, Ni-ZIF@rGO. Finally, the hierarchical Ni QD@NC@rGO composites could be fabricated by a one-step pyrolyzation of Ni-ZIF@rGO precursor at 450 °C for 2 h under flowing Ar gas. During the pyrolysis process, the Ni^{2+} ions liberated from Ni-ZIF nanoplates are reduced to defective Ni QDs, while the coordinated organic ligands not only convert into a thin-layer N-doped carbon (NC) but also provide the injection of N atoms into the rGO during the carbonization. Meanwhile, benefiting from the pinning effect of NG sheet, these Ni QDs encapsulated by NC are uniformly bonded with rGO sheet.

Fig. 1a shows the panoramic field-emission scanning electron microscopy (FESEM) images of the Ni-ZIF@rGO precursor. It can be observed that the surfaces of graphene sheet are covered by a large number of 2D nanoplates. The magnified FESEM images (Fig. 1b and c) further show that these 2D nanoplates with an average lateral size of about 80 nm have a smooth surface, and most of them tightly and densely lie on the graphene sheet, suggesting the possible strong interaction between the metal (Ni) species in Ni-ZIFs and the carboxylic groups of graphene surface. To further confirm this point, the morphology of the Ni-ZIF@rGO precursor after continuous sonication 2 h was checked and the results show that the precursors still maintain the

original morphology without detaching of Ni-ZIFs nanoplates from graphene sheet (Fig. S1). Interestingly, the macro-digital images of the as-prepared products also show the lamellar morphology (Fig. 1d), further corroborating the 2D feature of Ni-ZIF@rGO precursor. Fig. 1e gives the XRD pattern of the as-prepared Ni-ZIF@rGO precursor. Two major peaks positioned at 12.2° and 25.1° can be clearly observed, quite analogous to those of previously reported 2D Co-ZIFs (ZIF-67) except that the peaks slightly shift towards the lower angle probably caused by the larger ionic radius (0.69 Å) of Ni^{2+} than that (0.65 Å) of Co^{2+} [53]. Such a result strongly implies a possible similar crystal structure between our 2D Ni-ZIFs and the reported 2D Co-ZIFs. Rietveld refinement of the XRD pattern was further employed to elucidate the structure model of 2D Ni-ZIF@rGO. As shown in the inset in Fig. 1e, the fitted data is well matched with the observed one and the refined lattice parameters ($a = 17.37(3) \text{ \AA}$) of 2D Ni-ZIF are indeed slightly larger than those ($a = 16.93 \text{ \AA}$) of 2D Co-ZIF, demonstrating above results. Noted that no characteristic peaks of graphene were found in the XRD pattern of Ni-ZIF@rGO precursor, which may be ascribed to the high dispersion state of graphene [63]. Fig. 1f further illustrates the crystal structure of 2D Ni-ZIF, in which fourfold N-coordinated Ni centers surrounded by carbon skeleton network shows a preferential growth along (211) crystal plane. The detailed microstructure of 2D Ni-ZIF@rGO was further characterized by transmission electron microscope (TEM). Being consistent with the FESEM observations, many nanoplates evenly overlay on the surface of graphene (Fig. 1g). More TEM images in Fig. S2 further reveal that these nanoplates are ultrathin with the thickness ranging from 2~8 nm. Noted that although these 2D

nanoplates are sensitive to electron beam, some undamaged parts under high-resolution TEM (HRTEM) observation show the lattice fringes with an interplanar distance of 0.707 nm, corresponding to the (211) crystallographic planes of Ni-ZIF phase (Fig. 1h). The energy dispersive X-ray (EDX) mapping results confirm the uniform distribution of Ni, C and N within the 2D Ni-ZIF@rGO precursor (Fig. 1i-l). To the best of our knowledge, this is the first report on the synthesis of Ni-ZIF with well-defined 2D morphology. For comparison, we have also made an attempt to synthesize the pristine Ni-ZIF at the similar conditions, however, the XRD pattern of the products shows that in addition to the Ni-ZIF phase, Ni(OH)₂ phase can be apparently identified (Fig. S3). Such a result implies that the presence of rGO contributes to the formation of Ni-ZIF phase, which might be due to the ultralow lattice mismatch (~0.7%) between the exposed (002) plane of rGO and the preferential growth (211) plane of Ni-ZIF (Fig. 1h), being in favor of the heteroepitaxial growth of Ni-ZIF nanoplates on the rGO nanosheets [64]. The thermal stability of 2D Ni-ZIF@rGO precursor was investigated by thermogravimetric analysis (TGA). As shown in Fig. S4, the precursor underwent an apparent weight loss when heating to ~300 °C in nitrogen gas, showing less stable than previously reported ZIF-67 or ZIF-8 [65,66]. On the basis of TGA results, the as-synthesized 2D Ni-ZIF@rGO was heated at 350, 450, 550 °C to obtain the final products, respectively.

To examine the phase evolution during the pyrolysis, the XRD pattern of the thermal-annealed Ni-ZIF@rGO precursor at 450 °C (denoted as A-Ni-ZIF@rGO-450) is firstly given in Fig. 2a, from which only Ni phase and graphitic carbon can be observed, indicating an utter phase conversion from precursors to Ni and C after pyrolysis. Noticeably, both electron paramagnetic resonance (EPR) spectra and Rietveld refinement result suggest the possible existence of vacancies in Ni crystal (detailed information can be seen in Fig. S5, Fig. S6, Table S1 and S2). To further elucidate the effect of pyrolysis temperatures on the Ni phase structure, the XRD patterns of thermal-annealed Ni-ZIF@rGO precursor at 350 and 550 °C (denoted as A-Ni-ZIF@rGO-350 and A-Ni-ZIF@rGO-550, respectively) are given in Fig. S7. Obviously, the diffraction peaks of Ni phase become sharper with increasing pyrolysis temperature, indicating the crystal growth of Ni phase. Raman spectra of thermal-annealed Ni-ZIF@rGO at different temperatures were presented in Fig. 2b. It can be found that the relative intensity ratio of D to

G-band (I_D/I_G) slightly increases in the order of A-Ni-ZIF@rGO-350 < A-Ni-ZIF@rGO-450 < A-Ni-ZIF@rGO-550, indicating the formation of more carbon defects with increasing pyrolysis temperature [40]. The specific surface area and pore-size distribution of the A-Ni-ZIF@rGO-450 composites are further analyzed by the Brunauer-Emmett-Teller (BET) and Barrett-Joyner-Halenda (BJH) method, respectively. Fig. 2c presents the nitrogen adsorption–desorption isotherms, which can be extracted two parts, *i.e.*, the gradual uptakes at high pressure (0.45–1.0) accompanied with the hysteresis loops and the sharp uptakes at the relative lower pressure (< 0.05), implying the co-existence of mesopores and micropores [44]. This result is further confirmed by the pore size distribution (Fig. 2c inset), in which the pore sizes are mainly centered around 2 nm and ranges from 5 to 20 nm. The BET surface area and pore volume of A-Ni-ZIF@rGO-450 are calculated as 148 m² g⁻¹ and 0.266 cm³ g⁻¹, respectively. Such a specific surface area with affluently hierarchical pores is believed to be beneficial to exposing the catalytic sites and improving the mass transfer ability, leading to enhanced electrocatalytic activity [35,53,67]. In addition, thermogravimetric analysis (TGA) indicates that the loading amount of Ni in A-Ni-ZIF@rGO-450 composites is as high as about 60% (Fig. S8), which may provide sufficient chance for the generation of abundant catalytic active sites.

To investigate the surface and chemical states of elements, the X-ray photoelectron spectroscopy (XPS) analysis is performed for the A-Ni-ZIF@rGO-450 composite. Fig. 2d gives the high-resolution N 1s spectrum of the as-prepared A-Ni-ZIF@rGO-450 composite. The deconvoluted three peaks in N 1s spectrum correspond to graphitic–N (402.4 eV), Ni–N (399.3 eV), and pyridinic–N (397.6 eV), respectively, all of which contribute to the catalytic activity [43]. Particularly, the metal (Ni)–N bond has been confirmed as the most efficient active sites for the catalytic activity [45]. By further analysis of the high-resolution C 1s spectrum (Fig. 2e), it could be seen the peak of C–N and C=N bonds, suggesting the successful doping of N into C. As an evidence of the presence of metallic Ni, a high-resolution Ni 2p spectrum is given in Fig. 2f and it shows characteristic peaks of Ni metal at 852.6 (Ni 2p_{3/2}) and 869.8 eV (Ni 2p_{1/2}). The existence of apparent satellite peaks suggests the partial oxidation of Ni surface due to the exposure of sample under air or the interplay between the Ni metal and carboxylic

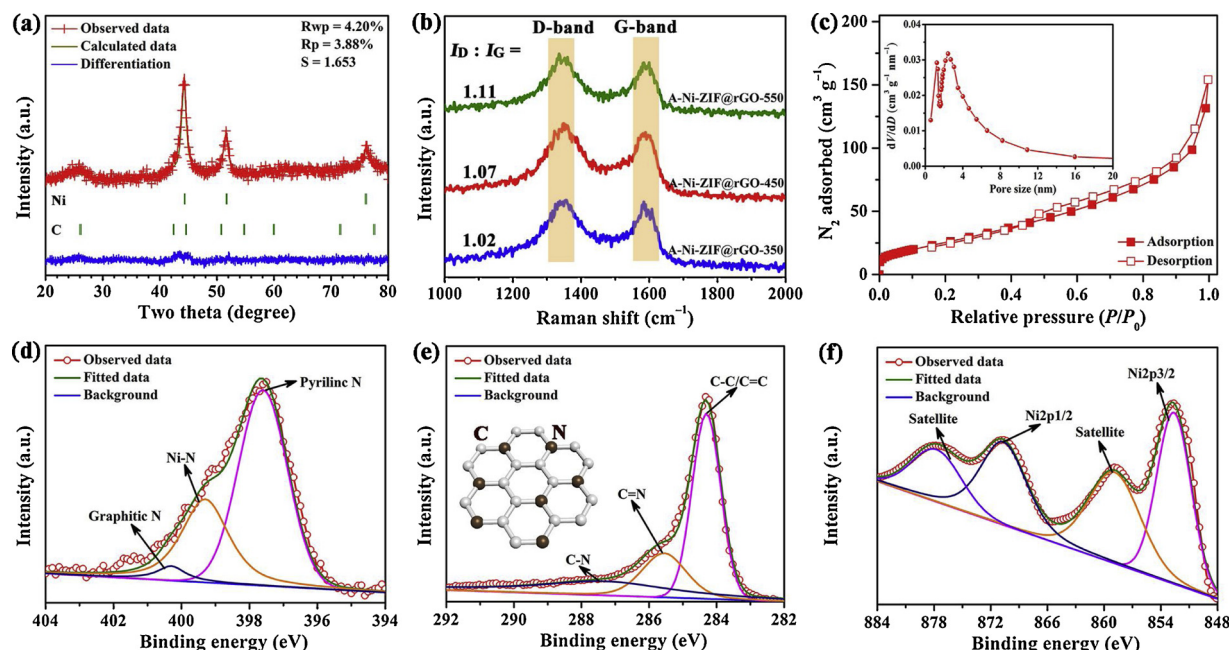


Fig. 2. (a) Rietveld refinement of XRD pattern, (c) specific surface area, and high-resolution (d) N 1s, (e) C 1s, and (f) Ni 2p XPS spectra of A-Ni-ZIF@rGO-450 composites; (b) Raman spectra of Ni-ZIF@rGO, A-Ni-ZIF@rGO-350, A-Ni-ZIF@rGO-450 and A-Ni-ZIF@rGO-550 composites. Inset in Fig. 2e: the atomic model of N-doping into carbon.

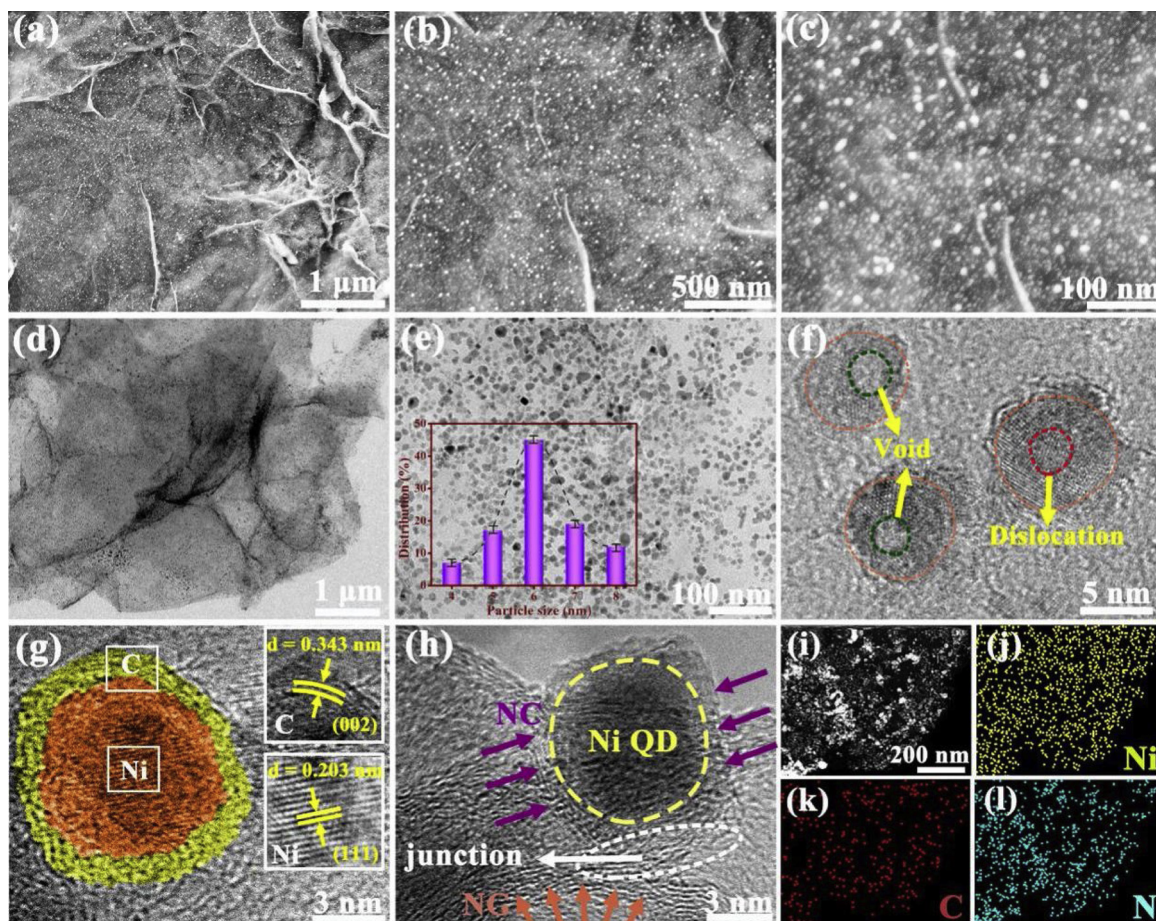


Fig. 3. (a–c) FESEM images, (d, e) TEM images, (f–h) high-resolution TEM images of Ni QD@NC@rGO composites; (i) HAADF-STEM image of the representative Ni QD@NC@rGO composite and corresponding (j) Ni, (k) C, and (l) N elemental mapping. Inset in Fig. 3e: the particle size distribution of Ni@NC subunit.

groups of graphene.

To reveal the morphological change during pyrolysis, Fig. 3a–c shows the FESEM images of the representative A-Ni-ZIF@rGO-450 composites. The low-magnification FESEM image (Fig. 3a) presents the rough surface of the graphene sheet. The magnified FESEM images (Fig. 3b and c) further indicate that large numbers of ultrasmall nano-subunits are uniformly anchored on the surface of graphene sheets. The presence of such nano-subunits also could effectively mitigate the stacking of graphene induced by strong Vander Waals interactions, preserving the intrinsic property of graphene. The microstructure of A-Ni-ZIF@rGO-450 composites is elucidated by TEM and high-angle annular dark-field scanning TEM (HAADF-STEM) images, showing that the uniformly anchored nano-subunits on the surface of curved graphene sheet have an average size of 6 nm (Fig. 3d and e). HRTEM image further reveals that these nano-subunits are composed of the nickel QDs wrapped by a few carbon layers (Fig. 3f and 3g). The interspacing of 0.204 nm in the QDs and 0.340 nm in the shell part are corresponding to the (111) and (002) lattice planes of Ni (rendered by yellow color) and carbon phases (rendered by purple color), respectively. Remarkably, the crystal defects such as void (vacancy) and/or lattice distortion can be clearly observed in nearly all the QDs (More TEM images can be seen in Fig. S9). The formation of rich defects in Ni QDs is probably related to following two aspects. One is the lattice strain induced by the dual carbon confinement towards Ni crystals during pyrolysis, which usually results in the formation of lattice distortion and vacancy [68]. The other is the intrinsically coordinated unsaturated Ni sites in the 2D Ni-ZIF, which might also contribute to the formation of vacancy in Ni crystals during pyrolysis [50]. The presence of crystal defects with low free energy is believed to not only create more exposed

active sites but also promote the adsorption of the H^* and/or OH^- intermediates. Fig. 3h further depicts the *in-situ* coupled junction between graphene and graphitic carbon. Noted that the domain rendered with white dotted oval (marked with white arrow) is possibly a feature property of covalent bonds between graphene and graphitic carbon, which is well in agreement with the previous results [69,70]. To further affirm the interaction between graphene and graphitic carbon, FESEM images of A-Ni-ZIF@rGO-450 after ultrasonication 2 h in ethanol were examined and displayed in Fig. S10. Obviously, the nano-subunits are still anchored well on graphene even suffered from powerful ultra-sonication, suggesting their chemical linkage with graphene rather than physical attachment on the surface of graphene. A HAADF-STEM image of representative A-Ni-ZIF@rGO-450 composites shows an even distribution of bright subunits, suggesting that the Ni QDs are highly confined and homogeneously dispersed on graphene sheet (Fig. 3i). The corresponding elemental mapping result suggests the co-existence and the uniform dispersion of Ni, C, and N elements within the composites (Fig. 3j–l). Based on the previous characterization results, herein, the A-Ni-ZIF@rGO-450 composites is denoted as Ni QD@NC@rGO.

Encouraged by the dedicate structure and expected compositions, the electrocatalytic performance of the as-prepared Ni QD@NC@rGO catalyst was evaluated using a three-electrode cell. The catalytic activity of Ni QD@NC@rGO towards OER was firstly assessed in 1.0 M KOH. Fig. 4a gives the linear sweep voltammetry (LSV) curve of the Ni QD@NC@rGO towards the OER. For comparison purpose, the LSV curves of A-rGO-450, A-Ni-ZIF@rGO-350, and A-Ni-ZIF@rGO-550 catalysts are also shown in Fig. 4a. Notably, the Ni QD@NC@rGO catalyst requires the lowest overpotential (265 mV) to drive the current density of 10 mA cm^{-2} among the investigated catalysts (Fig. S11), which is

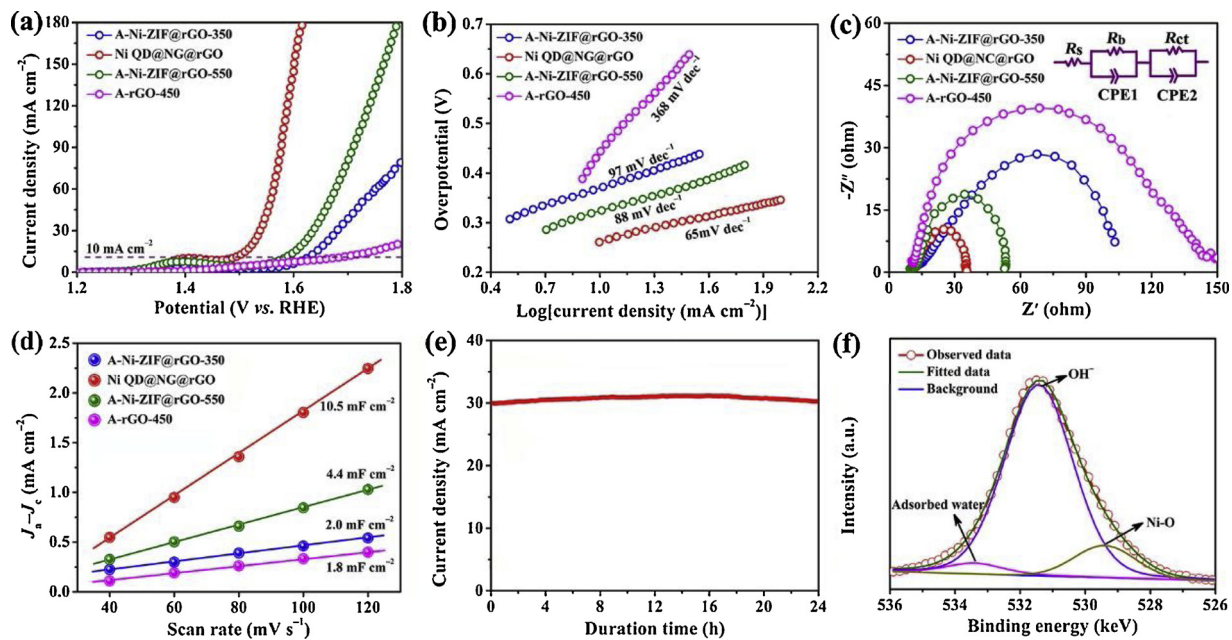


Fig. 4. (a) LSV curves, (b) Tafel slopes, (c) EIS spectra, and (d) C_{dl} values of A-rGO-450, A-Ni-ZIF@rGO-350, Ni QD@NC@rGO, and A-Ni-ZIF@rGO-550 electrodes for OER; (e) the current–time curve of Ni QD@NC@rGO at controlled potential; (f) the high-resolution O 1 s XPS spectrum in the cycled Ni QD@NC@rGO. Inset in Fig. 4c: the simulated equivalent circuit according to the EIS spectra.

also lower than that (323 mV) of the commercial IrO_2 @C catalyst (Fig. S12) and most previously reported TMs@NC catalysts (Table S3), demonstrating its advantage as an OER catalyst. The catalytic OER kinetics of the catalysts were investigated by linear fitting Tafel plots derived from LSV curves. As shown in Fig. 4b, the Tafel slope of Ni QD@NC@rGO (65 mV dec⁻¹) is also smaller than those of A-Ni-ZIF@rGO-350 (97 mV dec⁻¹), A-Ni-ZIF@rGO-550 (88 mV dec⁻¹) and A-G-450 (368 mV dec⁻¹) catalysts, indicating more favorable OER catalytic kinetics on the Ni QD@NC@rGO in alkaline electrolyte. The superior OER catalytic activity of Ni QD@NC@rGO to those of A-Ni-ZIF@rGO-350 and A-Ni-ZIF@rGO-550 could be attributed to the appropriate pyrolysis temperature, which assured the optimum balance among the particle size, graphitization degree of carbon, specific surface area, the nitrogen doping amount and the thickness of carbon shell. For example, on the one hand, upon increasing the pyrolysis temperature, the thickness of carbon shell surrounding the Ni particles gradually decreases in the order of A-Ni-ZIF@rGO-350 (several amorphous carbon layers) > A-Ni-ZIF@rGO-450 (3~5 graphitic carbon layers) > A-Ni-ZIF@rGO-550 (1~3 graphitic carbon layers) (Fig. 3f-h and Fig. S13), implying the improved electron penetration ability against the pyrolysis temperature [13,42]. However, with the increase of the pyrolysis temperature, the obtained Ni particle size would become larger, leading to the low utilization ratio of active sites (Fig. 3f-h and Fig. S13) [45]. Thus, a moderate pyrolysis temperature is favorable for achieving the MOF-derived TMs@NC with high catalytic activity. Noted that to better demonstrate the synergistic advantage among the Ni QD, NC and rGO subunits, the catalytic activities of NC, NC@rGO, Ni/NiO@NC and Ni@C@rGO composites were also compared. As shown in Fig. S14, all of them exhibited an inferior OER activity as compared to that of Ni QD@NC@rGO (e.g., the overpotentials at the current density of 10 mA cm⁻² for NC, NC@rGO, Ni/NiO@NC, and Ni@C@rGO are 433, 415, 387, and 353 mV, respectively), strongly demonstrating the subunit coupling in improving the catalytic activity.

To gain further insight into the high OER catalytic performance of Ni QD@NC@rGO, the electrochemical impedance spectroscopy (EIS) and the electrochemical surface area (ECSA) of the catalysts were analyzed. Nyquist plots are shown in Fig. 4c and the simulated equivalent circuit is displayed in the insets in Fig. 4c. On the basis of the

extracted values of charge transfer resistance (R_{ct}) (Fig. S15), it can be known that Ni QD@NC@rGO has the smaller R_{ct} value (20.2 Ω) than those of A-Ni-ZIF@rGO-350 (78.4 Ω), A-Ni-ZIF@rGO-550 (38.6 Ω) and A-G-450 (82.3 Ω), revealing its stronger charge transfer ability during OER process. The ECSA of catalysts can be directly reflected from the double-layer capacitance (C_{dl}) by deriving from the cyclic voltammetry (CV) curves versus the scan rate (Fig. S16). The Ni QD@NC@rGO has the largest C_{dl} value (10.5 mF cm⁻²) among the investigated catalysts (Fig. 4d), suggesting its enriched and more potential catalytically active sites for electrocatalysis during OER. As another important criterion to evaluate the advantages of electrocatalyst, the long-term durability of the Ni QD@NC@rGO catalysts is assessed by controlled potential electrolysis. As shown in Fig. 4e, the catalyst shows the impressive operational stability (negligible decay after 24 h at a current density of 30 mA cm⁻²).

The microstructure of Ni QD@NC@rGO after OER duration test is characterized by TEM. As shown in Fig. S17a and S17b, the original morphology can be well maintained after cycling. Nevertheless, the HRTEM observation (Fig. S17c) indicates that minor NiOOH phase is formed on the surface of some Ni particle. The selected area electron diffraction (SAED) pattern further confirms the co-existence of Ni and NiOOH phases (Fig. S17d). Such a finding is also in line with the XPS analysis of the elements in the cycled Ni QD@NC@rGO. As shown in Fig. S18, the high-resolution Ni 2p XPS spectrum indicates the partial oxidation on the surface of Ni particle during OER process. This result could be further corroborated by the high-resolution O 1 s XPS spectrum (Fig. 4f), in which the peaks positioned at 529.3, 531.2, and 533.1 eV should be assigned to the typical Ni-O bonds, protonated oxygen from H_2O or O_2 , and the adsorbed water/oxygen molecular, respectively. As previous reports demonstrated, the surface oxidation layer formed on the non-oxide TM-based catalysts would become steady during the prolonged OER tests, resulting in the formation of interface between them. Such interfaces have demonstrated to be beneficial for lowering the Gibbs free energy of the reaction intermediate during OER process [71,72].

To examine the bifunctional activity, the HER performance of Ni QD@NC@rGO is also evaluated and compared with those of A-rGO-450, A-Ni-ZIF@rGO-350, A-Ni-ZIF@rGO-550, and Pt@C in the same

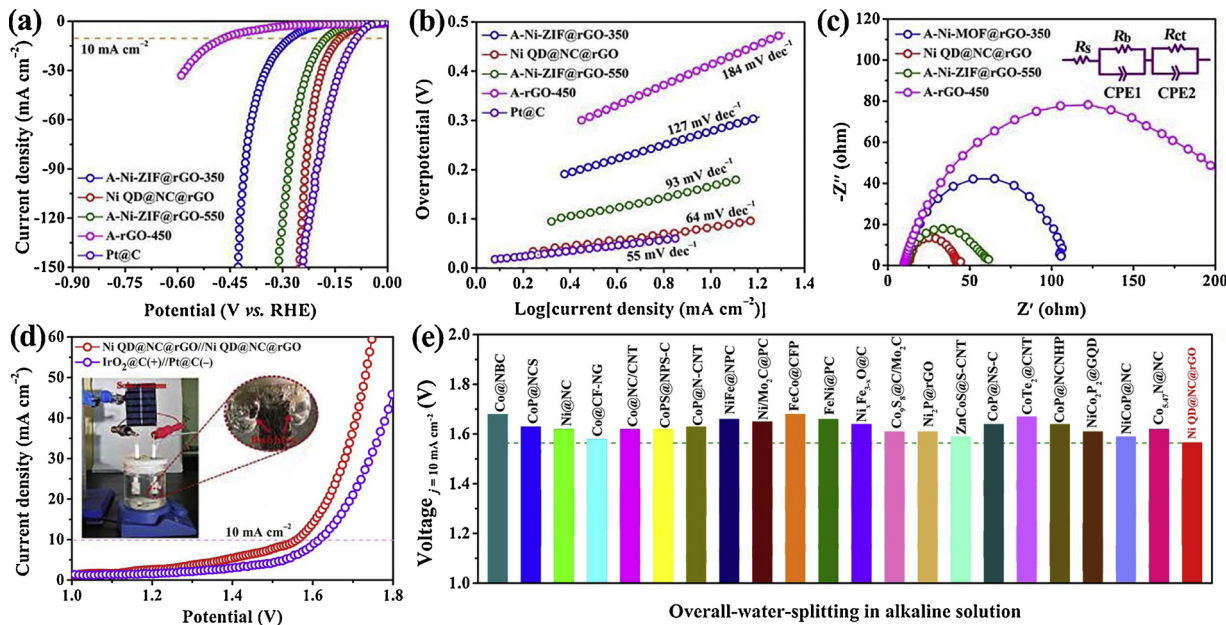


Fig. 5. (a) LSV curves and (b) Tafel slopes of A-rGO-450, A-Ni-ZIF@rGO-350, Ni QD@NC@rGO, A-Ni-ZIF@rGO-550 and Pt@C electrodes for HER, (c) EIS spectra of A-rGO-450, A-Ni-ZIF@rGO-350, Ni QD@NC@rGO, and A-Ni-ZIF@rGO-550 electrodes; (d) the polarization curves of Ni QD@NC@rGO//Ni QD@NC@rGO and $\text{IrO}_2@C(+)//\text{Pt}@C(-)$ for overall water splitting; (e) comparison of the cell voltages to drive a current density of 10 mA cm^{-2} for the Ni QD@NC@rGO with recently reported transition metal–carbon-based bifunctional catalysts. Inset in Fig. 5c: the simulated equivalent circuit according to the EIS spectra; Inset in Fig. 5d: digital image of overall water splitting configuration driven by solar energy in 1.0 M KOH.

electrolyte. The polarization curves in Fig. 5a show that the Ni QD@NC@rGO has the overpotential (133 mV) at the current density of 10 mA cm^{-2} , much smaller than those of the A-G-450 (465 mV), A-Ni-ZIF@rGO-350 (275 mV), A-Ni-ZIF@rGO-550 (174 mV) (Fig. S19). Furthermore, the performance is even close to that of commercial Pt/C catalyst (Fig. 5a) and also superior to those of most previously TMs@NC electrocatalyst (Table S4). The Tafel slope of Ni QD@NC@rGO is 64 mV dec^{-1} , which is associated with Volmer–Heyrovsky mechanism for hydrogen production (Fig. 5b). EIS analysis is then performed to gain further insight into the electrocatalytic HER process and the corresponding Nyquist plots are shown in Fig. 5c. Similar to the OER case, the simulated results also show that the Ni QD@NC@rGO possesses the strongest charge transfer ability during the HER process (inset in Fig. 5c and Fig. S20). In addition, all of NC, NC@rGO, Ni/NiO and NC@rGO composites show an inferior HER activity as compared to that of Ni QD@NC@rGO (Fig. S21), demonstrating again the subunit coupling in improving the catalytic activity. The cycle duration test also demonstrates the high stability of Ni QD@NC@rGO in the alkaline solution (Fig. S22).

Inspired by the excellent OER and HER performance of Ni QD@NC@rGO, an electrolyzer was assembled in a two-electrode configuration using the Ni QD@NC@rGO catalyst as the both the anode and cathode for overall water splitting in 1.0 M KOH. Remarkably, as revealed in Fig. 5d, the Ni QD@NC@rGO catalysts drive a current density of 10 mA cm^{-2} at the cell voltage of as low as 1.563 V, substantially lower than that of the state-of-the-art $\text{Pt}@C||\text{IrO}_2@C$ couple (1.614 V) (Fig. 5d) and also outperforms most recently reported transition-metal-based bifunctional electrocatalysts for overall water splitting (Fig. 5e and Table S5). Noted that when we cast the as-synthesized electrocatalysts onto the glass carbon, the overpotentials for HER and OER to afford 10 mA cm^{-2} are 133 and 265 mV, respectively. Correspondingly, the cell voltage for overall water electrolysis is theoretically 1.628 V. While under practical two-electrode configuration, the cell voltage is only 1.563 V. Such discrepancy could be also commonly observed in previous studies [42,53,73–75], which is attributed to the following three aspects. One is the larger mass loading (1 mg cm^{-2}) in the two-electrode configuration than that (0.71 mg cm^{-2}) in the three-electrode

configuration, which greatly boost the catalytic activities [76,77]. Another is that using the carbon cloth as substrate instead of glass carbon ensures high electric conductivity, favorable surface area and rich interlinked macropores, thus greatly promoting the electron penetration, active sites exposing as well as mass transfer ability [38]. In addition, the carbon cloth also contribute to a certain catalytic activity during water splitting [78] (Fig. S23). On the other hand, the cyclic LSV test was performed, as shown in Fig. S24, the LSV curve after 300 cycles is basically overlapped with the first one, exhibiting a rather high stability. Since 30 wt. % KOH basic solution is commonly used in the commercial water electrolyzer, the overall water splitting performance in this electrolyte has also been evaluated. As shown in LSV and *i-t* curves (Fig. S25a and Fig. S25b), the bifunctional Ni QD@NC@rGO electrocatalysts not only possessed a low overpotential of 350 mV at the current density of 10 mA cm^{-2} , but also showed a slight current decay after 24 h, further demonstrating its potential application. Additionally, the water splitting configuration constructed by using the Ni QD@NC@rGO catalysts can also be effectively operated by coupling with solar energy system (Fig. 5d inset), showing great promise in future energy conversion application. To determine the Faradaic efficiency (FE), we compared the amount of experimentally quantified gas with theoretically calculated gas (assuming 100% FE) using the chronopotentiometric reaction. As shown in Fig. S26, the anode/cathode shows stable oxygen/hydrogen evolution rates that quite match well with theoretical values, implying a nearly 100% FE for both OER and HER processes.

Density functional theory (DFT) calculations on the intermediate H^* adsorption free energies (ΔG , * represents an adsorption site) and charge density redistributions of several configurations, including Ni, $\text{Ni}@C$, $\text{Ni}@N_1C_{31}$, $\text{Ni}@N_2C_{30}$, and $\text{Ni}_x@N_2C_{30}$, were systematically performed to reveal the synergistic nature among the N, C and defective Ni clusters during water splitting. Theoretically, an ideal HER catalyst possesses a ΔG value of approach to 0, which is beneficial for both the H^* adsorption and desorption [29]. Fig. 6a compared the ΔG values of various modeled catalysts during HER. Different from the weak H^* adsorption ability of bare graphene (ΔG is $\sim 1.9 \text{ eV}$) as our previous work calculated [45], the H^* adsorption of bare Ni is too strong (ΔG is $\sim 0.45 \text{ eV}$), showing the poor activity toward HER. Nevertheless, upon

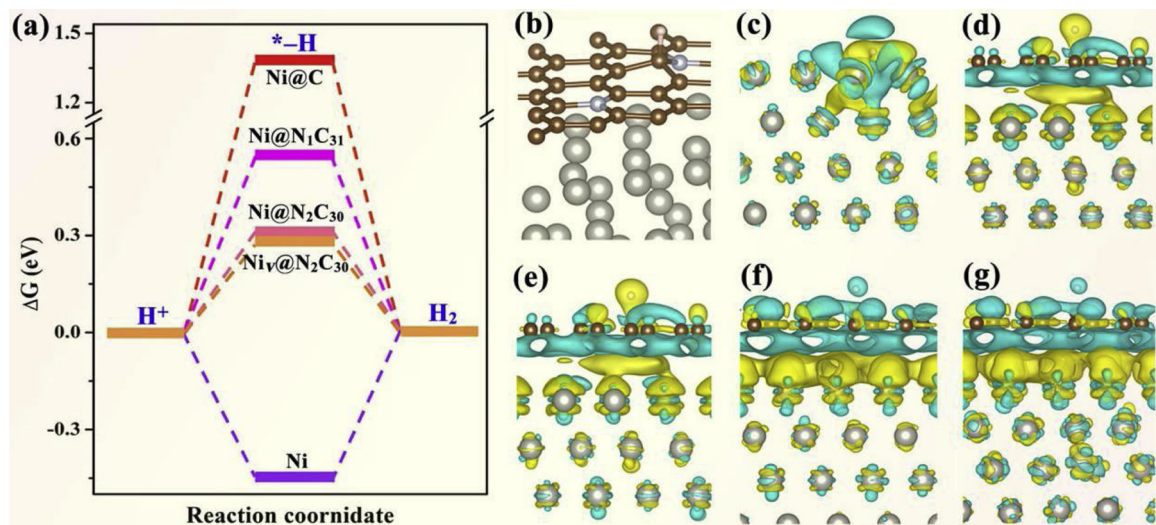


Fig. 6. (a) The calculated free-energy diagram of the HER on Ni, Ni@C, Ni@N₁C₃₁, Ni@N₂C₃₀, and Ni_V@N₂C₃₀; (b) calculated model of Ni@N₂C₃₀; the charge density redistributions (charge transfer between Ni/Ni_V and C–H/N–C–H) of (b) Ni–H, (c) Ni@C–H, (d) Ni@N₁C₃₁–H, (e) Ni@N₂C₃₀–H and (f) Ni_V@N₂C₃₀–H systems (Atoms with grey, brown, white, and pink colors represent Ni, C, N and H atoms, respectively; in charge density isosurface plot, the blue and yellow isosurfaces show the electron losing and gaining, respectively) (For interpretation of the references to colour in this figure legend, the reader is referred to the web version of this article).

hybridizing Ni with graphene, the ΔG value can be remarkably tuned. The calculations (Fig. 6a) show that the graphene absorbents, Ni@C, has a ΔG of ~1.4 eV, which is lower than the case of bare graphene, but still too weak to facilitate the HER. Incorporating the N into the graphene layer can significantly reduce the ΔG to ~0.55 eV when N concentration is at ~3% (1 N per 32 C sites). Further increase the N concentration to ~6% (1 N per 16 C sites) can bring the ΔG the even small value of ~0.30 eV, hence the HER will be greatly enhanced by introducing the N into the system. As shown by the systematic DFT evaluations, the introducing of N doped graphene helps the HER, and the H* adsorption free energies, ΔG , approach to smaller values (close to zero) when increasing N composition. It is possible that the HER can be greatly boosted by tuning the N concentration to a proper range, as observed in the experiment. The computational investigations also change the Ni slab to porous Ni slab, by removing 10% of the Ni atoms in the system, can also modify the HER slightly (reduced the ΔG to 0.28 eV in this case). To further unveil the synergistic mechanism of the graphene, N and Ni vacancy, Fig. 6c–g shows the charge redistributions (charge transfer between C–N–H and Ni substrate) of Ni–H, Ni@C–H, Ni@N₁C₃₁–H, Ni@N₂C₃₀–H and Ni_V@N₂C₃₀–H systems, respectively. Previous studies have proved that catalytic reaction mainly germinates at the graphene surface in the TMs@NC catalysts [30,33]. Thus, a favorable electron distribution of graphene layer plays a crucial role in high catalytic activity towards HER or OER. Nonetheless, as shown in Fig. 6c, a strong electron interaction occurs between Ni and H*, suggesting that Ni species also can function as the electrocatalytically active sites. In addition, the construction of hetero-interface between Ni core and C shell also induces a charge transfer from Ni to carbon layer (Fig. 6d), modifying the π -conjugated system of carbon and generating the in-plane charge polarization on the surface of carbon, leading to the improved C–H binding energy. Based on Ni@C model, further nitrogen doping renders the C layer *n*-type-doped and rebalances the charge density of the Ni@C–H system (Fig. 6e and f), leading to the tunable adsorption ability of Ni@C model to H. Furthermore, based on the Ni@N₂C₃₀ model, the introduction of some vacancies in Ni core causes the strain or ligand effects (Fig. 6g), accelerating its charge transfer from Ni core to C layer, which is beneficial for enhancing C–H binding strength. Therefore, the engineering of the N species doping, Ni–C conjugation, and atomic defects can effectively optimize the catalytic activity.

To demonstrate the general versatility of developed strategy, it is

explored to synthesize binary TM QD@NC@rGO. For instance, we have successfully synthesized binary Ni–Co QD@NC@rGO composite using the similar strategy. As expected, to achieve the current density of 10 mA cm⁻², it only requires low overpotentials of 251 and 113 mV for OER and HER in 1.0 M KOH, respectively, exhibiting excellent electrocatalytic performance (Fig. S27).

4. Conclusions

In summary, we have developed a novel 2D hybrid composites consisting of N-doped thin-layer carbon-encapsulated defective Ni QD anchored on the surface of graphene sheets via a low-temperature pyrolysis of graphene-wrapped 2D Ni-ZIF nanoplates. The optimized Ni QD@NC@rGO catalyst shows superior OER and HER activity to most previously reported TMs@NC catalysts in the alkaline solution. Remarkably, it enables an alkaline electrolyzer with a current density of 10 mA cm⁻² at an ultralow cell voltage of 1.563 V for overall water splitting. Both experiments and theoretical calculations indicate that the excellent activity of Ni QD@NC@rGO catalyst can be attributed to the following factors: i) a large accessible active sites due to the 2D structure and highly dispersed Ni QD; ii) the improved intrinsic activity of active sites and optimal Gibbs free energy of adsorption caused by the electronic regulation via coupled NC and introduced defects within QDs; iii) the favourable electron/ion transport as well as gas generation and release from the intimate contact of 2D active nanosheets on conductive graphene and hierarchically porous structure. Moreover, the developed strategy in this study can be easily applied to synthesize other binary TMs QD@NC@rGO catalysts and may open a new avenue for constructing effective bifunctional TMs-based electrocatalyst for overall water splitting.

Acknowledgements

This work was financially supported by the National Natural Science Foundation of China (Grant Nos. 51672049 and 51871060), Research Grant for Talent Introduction of Fudan University, China (Grant No. JJH2021103), the China Postdoctoral Science Foundation (Grant No. 2018M640337) and the Recruitment Program of Global Youth Experts (National Thousand Young Talents Program).

Appendix A. Supplementary data

Supplementary material related to this article can be found, in the online version, at doi:<https://doi.org/10.1016/j.apcatb.2019.03.032>.

References

[1] Y.F. Liu, K. Zhong, K. Luo, M.X. Gao, H.G. Pan, Q.D. Wang, Size-dependent kinetic enhancement in hydrogen absorption and desorption of the Li-Mg-N-H system, *J. Am. Chem. Soc.* 131 (2009) 1862–1870.

[2] M.Y. Zheng, K.L. Guo, W.J. Jiang, T. Tang, X.Y. Wang, P.P. Zhou, J. Du, Y.Q. Zhao, C.L. Xu, J.S. Hu, When Mo₂ meets FeOOH: a “one-stone-two-birds” heterostructure as a bifunctional electrocatalyst for efficient alkaline water splitting, *Appl. Catal. B: Environ.* 244 (2019) 1004–1012.

[3] Y.P. Pang, Y.F. Liu, M.X. Gao, L.Z. Ouyang, J.W. Liu, H. Wang, M. Zhu, H.G. Pan, A mechanical-force-driven physical vapour deposition approach to fabricating complex hydride nanostructures, *Nat. Commun.* 5 (2014) 1–9.

[4] M.A.R. Anjum, M.S. Okayay, M.K. Kim, Min Hee Lee, N. Park, J.S. Lee, Bifunctional sulfur-doped cobalt phosphide electrocatalyst outperforms allnoble-metal electrocatalysts in alkaline electrolyzer for overall water splitting, *Nano Energy* 53 (2018) 286–295.

[5] Y.F. Liu, H.G. Pan, M.X. Gao, Q.D. Wang, Advanced hydrogen storage alloys for Ni/MH rechargeable batteries, *J. Mater. Chem.* 21 (2011) 4743–4755.

[6] Q.C. Xu, H. Jiang, H.X. Zhang, Y.J. Hu, C.Z. Li, Heterogeneous interface engineered atomic configuration on ultrathin Ni(OH)₂/Ni₃S₂ nanoforest for efficient water splitting, *Appl. Catal. B: Environ.* 242 (2019) 60–66.

[7] J. Wang, F. Xu, H. Jin, Y. Chen, Y. Wang, Non-noble metal-based carbon composites in hydrogen evolution reaction: fundamentals to applications, *Adv. Mater.* 29 (2017) 1605838.

[8] A. Sivanantham, S. Shanmugam, Nickel selenide supported on nickel foam as an efficient and durable non-precious electrocatalyst for the alkaline water electrolysis, *Appl. Catal. B: Environ.* 203 (2017) 485–493.

[9] C.C.L. McCrory, S. Jung, I.M. Ferrer, S.M. Chatman, J.C. Peters, T.F. Jaramillo, Benchmarking hydrogen evolving reaction and oxygen evolving reaction electrocatalysts for solar water splitting devices, *J. Am. Chem. Soc.* 137 (2015) 4347–4357.

[10] Z.L. Chen, M. Liu, R.B. Wu, Strongly coupling of Co₃S₈/Zn-Co-S heterostructures rooted in carbon nanocages towards efficient oxygen evolution reaction, *J. Catal.* 361 (2018) 322–330.

[11] Z.L. Chen, R.B. Wu, M. Liu, Y. Liu, S.Y. Xu, Y. Ha, Y.H. Guo, X.B. Yu, D.L. Sun, F. Fang, Tunable electronic coupling of cobalt sulfide/carbon composites for optimizing oxygen evolution reaction activity, *J. Mater. Chem. A* 6 (2018) 10304–10312.

[12] R.B. Wu, D.P. Wang, K. Zhou, N. Srikanth, J. Wei, Z. Chen, Porous cobalt phosphide/graphitic carbon polyhedra hybrid composites for efficient oxygen evolution reactions, *J. Mater. Chem. A* 4 (2016) 13742–13745.

[13] K. Qu, Y. Zheng, Y. Jiao, X. Zhang, S. Dai, S.Z. Qiao, Polydopamine-inspired, dual heteroatom-doped carbon nanotubes for highly efficient overall-water-splitting, *Adv. Energy Mater.* 7 (2017) 1602068.

[14] Z.L. Chen, Y. Ha, Y. Liu, H. Wang, H.Y. Yang, H.B. Xu, Y.J. Li, R.B. Wu, In situ formation of cobalt nitrides/graphitic carbon composites as efficient bifunctional electrocatalysts for overall water splitting encapsulating, *ACS Appl. Mater. Interfaces* 10 (2018) 7134–7144.

[15] S. Anantharaj, S.R. Ede, K. Sakthikumar, K. Karthick, S. Mishra, S. Kundu, Recent trends and perspectives in electrochemical water splitting with an emphasis to sulphide, selenide and phosphide catalysts of Fe, Co and Ni: a review, *ACS Catal.* 6 (2016) 8069–8097.

[16] Z.K. Kou, L. Zhang, Y.Y. Ma, X.M. Ma, W.J. Zang, J. Zhang, S.Z. Huang, Y.H. Du, A.K. Cheetham, J. Wang, 2D carbide nanomeshes and their assembling into 3D microflowers for efficient water splitting, *Appl. Catal. B: Environ.* 243 (2019) 678–685.

[17] W. Ahn, M.G. Park, D.U. Lee, M.H. Seo, G.P. Jiang, Z.P. Cano, F.M. Hassan, Z.W. Chen, Hollow multivolt nanocuboids derived from ternary Ni-Co-Fe Prussian blue analog for dual-electrocatalysis of oxygen and hydrogen evolution reactions, *Adv. Funct. Mater.* 28 (2018) 1802129.

[18] Y.Q. Yang, W.B. Zhang, Y.L. Xiao, Z.P. Shi, X.M. Cao, Y. Tang, Q.S. Gao, CoNiSe₂ heteronanorod decorated with layered-double-hydroxides for efficient hydrogen evolution, *Appl. Catal. B: Environ.* 242 (2019) 132–139.

[19] H.G. Pan, Y.F. Liu, M.X. Gao, Y.F. Zhu, Y.Q. Lei, Q.D. Wang, An investigation on the structural and electrochemical properties of La_{0.7}Mg_{0.3}(Ni_{0.85}Co_{0.15})_x (x = 3.15–3.80) hydrogen storage electrode alloys, *J. Alloys. Compd.* 351 (2003) 228–234.

[20] S.M. Zhang, H.T. Gu, H.G. Pan, S.H. Yang, W.B. Du, X. Li, M.X. Gao, Y.F. Liu, M. Zhu, L.Z. Ouyang, D.C. Jian, F. Pan, A novel strategy to suppress capacity and voltage fading of Li- and Mn-rich layered oxide cathode material for lithium-ion batteries, *Adv. Energy Mater.* 7 (2017) 1601066.

[21] J.H. Wang, W. Cui, Q. Liu, Z.C. Liu, A.M. Asiri, X.P. Sun, Recent progress in cobalt-based heterogeneous catalysts for electrochemical water splitting, *Adv. Mater.* 28 (2016) 215–230.

[22] T.T. Liu, L.S. Xie, J.H. Yang, R.M. Kong, G. Du, A.M. Asiri, X.P. Sun, L. Chen, Self-standing Co₃P nanosheets array: a three-dimensional bifunctional catalyst electrode for overall water splitting in both neutral and alkaline media, *ChemElectroChem* 4 (2017) 1840–1845.

[23] J.Q. Tian, N.Y. Cheng, Q. Liu, X.P. Sun, Y.Q. He, A.M. Asiri, Self-supported NiMo hollow nanorod array: an efficient 3D bifunctional catalytic electrode for overall water splitting, *J. Mater. Chem. A* 3 (2015) 20056–20059.

[24] T.T. Liu, Q. Liu, A.M. Asiri, Y.L. Luo, X.P. Sun, An amorphous CoSe film behaves as an active and stable full water-splitting electrocatalyst under strongly alkaline conditions, *Chem. Commun.* 51 (2015) 16683–16686.

[25] C. Tang, R. Zhang, W.B. Lu, L.B. He, X. Jiang, A.M. Asiri, X.P. Sun, Fe-doped Co₃P nanoarray: a monolithic multifunctional catalyst for highly efficient hydrogen generation, *Adv. Mater.* 29 (2017) 1602441.

[26] W.X. Zhu, T.S. Zhang, Y. Zhang, Z.H. Yue, Y.G. Li, R. Wang, Y.W. Ji, X.P. Sun, J.L. Wang, A practical-oriented NiFe-based water-oxidation catalyst enabled by ambient redox and hydrolysis co-optimization strategy, *Appl. Catal. B: Environ.* 244 (2019) 844–852.

[27] D. Wu, Y.C. Wei, X. Ren, X.Q. Ji, Y.W. Liu, X.D. Guo, Z.A. Liu, A.M. Asiri, Q. Wei, X.P. Sun, Co(OH)₂ nanoparticle-encapsulating conductive nanowires array: room-temperature electrochemical preparation for high-performance water oxidation electrocatalysis, *Adv. Mater.* 30 (2018) 1705366.

[28] Z.C. Wang, H.L. Liu, R.X. Ge, X. Ren, D.J. Yang, L.X. Zhang, X.P. Sun, Phosphorus-doped Co₃O₄ nanowire array: a highly efficient bifunctional electrocatalyst for overall water splitting, *ACS Catal.* 8 (2018) 2236–2241.

[29] X. Zou, X. Huang, A. Goswami, R. Silva, B.R. Sathe, E. Mikmeková, Cobalt-embedded nitrogen-rich carbon nanotubes efficiently catalyze hydrogen evolution reaction at all pH values, *Angew. Chem. Int. Ed.* 53 (2014) 4372.

[30] W. Zhou, J. Zhou, Y. Zhou, J. Lu, K. Zhou, L. Yang, et al., N-doped carbon-wrapped cobalt nanoparticles on N-doped graphene nanosheets for high-efficiency hydrogen production, *Chem. Mater.* 27 (2015) 2026–2032.

[31] H. Fei, Y. Yang, Z. Peng, G. Ruan, Q. Zhong, L. Li, Cobalt nanoparticles embedded in nitrogen-doped carbon for the hydrogen evolution reaction, *ACS Appl. Mater. Interfaces* 7 (2015) 8083–8087.

[32] Y. Zhang, Y. Ma, Y.Y. Chen, L. Zhao, L.B. Huang, H. Luo, Encased copper boosts the electrocatalytic activity of N-doped carbon nanotubes for hydrogen evolution, *ACS Appl. Mater. Interfaces* 9 (2017) 36857–36864.

[33] Y. Yang, Z. Lin, S. Gao, J. Su, Z. Lun, G. Xia, Tuning electronic structures of non-precious ternary alloys encapsulated in graphene layers for optimizing overall water splitting activity, *ACS Catal.* 7 (2017) 469–479.

[34] R.B. Wu, D.P. Wang, J.Y. Han, H. Liu, K. Zhou, Y.Z. Huang, R. Xu, J. Wei, X.D. Chen, Z. Chen, A general approach towards multi-faceted hollow oxide composites using zeolitic imidazolate frameworks, *Nanoscale* 7 (2015) 965–974.

[35] Y. Pan, K.A. Sun, S.J. Liu, X. Cao, K.L. Wu, W.C. Cheong, Z. Chen, Y. Wang, Y. Li, Y.Q. Liu, D.S. Wang, Q. Peng, C. Chen, Y.D. Li, Core–shell ZIF-8@ZIF-67-derived Co₃P nanoparticle-embedded N-doped carbon nanotube hollow polyhedron for efficient overall water splitting, *J. Am. Chem. Soc.* 140 (2018) 2610–2618.

[36] Z.L. Chen, R.B. Wu, H. Wang, H.L. Zhang, Y. Song, F.L. Wu, F. Fang, D.L. Sun, Embedding ZnSe nanodots in nitrogen-doped hollow carbon architectures for superior lithium storage, *Nano Res.* 11 (2018) 966–978.

[37] H. Wang, Z.L. Chen, Y. Liu, H.B. Xu, L.C. Cao, H.L. Qing, R.B. Wu, Hierarchically porous-structured Zn_xCo_{1-x}S@C-CNT nanocomposites with high-rate cycling performance for lithium-ion batteries, *J. Mater. Chem. A* 5 (2017) 23221–23227.

[38] Z.L. Chen, R.B. Wu, H. Wang, Y.K. Jiang, L. Jin, Y.H. Guo, Y. Song, F. Fang, D.L. Sun, Construction of hybrid hollow architectures by *in-situ* rooting ultralfine ZnS nanorods within porous carbon polyhedra for enhanced lithium storage properties, *Chem. Eng. J.* 326 (2017) 680–690.

[39] R.B. Wu, D.P. Wang, X.H. Rui, B. Liu, K. Zhou, A.W.K. Law, Q.Y. Yan, Z. Chen, In-situ formation of hollow hybrid composed of cobalt sulfides embedded within porous carbon polyhedra/carbon nanotubes for high-performance lithium-ion batteries, *Adv. Mater.* 27 (2015) 3038–3044.

[40] R.B. Wu, Y.H. Xue, B. Liu, K. Zhou, J. Wei, S.H. Chan, Cobalt selenide nanoparticles embedded within nitrogen-doped porous carbon as advanced oxygen reduction reaction electrocatalyst, *J. Power Sources* 330 (2016) 132–139.

[41] Y. Li, B. Jia, Y. Fan, K. Zhu, G. Li, C.Y. Su, Bimetallic zeolitic imidazolate framework derived carbon nanotubes embedded with Co nanoparticles for efficient bifunctional oxygen electrocatalyst, *Adv. Energy Mater.* 7 (2017) 1702048.

[42] Y. Hou, Z. Wen, S. Cui, S. Ci, S. Mao, J. Chen, An advanced nitrogen-doped graphene/cobalt-embedded porous carbon polyhedron hybrid for efficient catalysis of oxygen reduction and water splitting, *Adv. Funct. Mater.* 25 (2015) 872.

[43] Y. Xu, W. Tu, B. Zhang, S. Yin, Y. Huang, M. Kraft, R. Xu, Nickel nanoparticles encapsulated in few-layer nitrogen-doped graphene derived from metal-organic frameworks as efficient bifunctional electrocatalysts for overall-water-splitting, *Adv. Mater.* 29 (2017) 1605957.

[44] T. Wang, Z. Kou, S. Mu, J. Liu, D. He, I.S. Amiinu, 2D dual-metal zeolitic-imidazolate-framework-(ZIF)-derived bifunctional air electrodes with ultrahigh electrochemical properties for rechargeable zinc-air batteries, *Adv. Funct. Mater.* 28 (2018) 1705048.

[45] Z.L. Chen, R.B. Wu, Y. Liu, Y. Ha, Y.H. Guo, D.L. Sun, M. Liu, F. Fang, Ultrafine Co nanoparticles encapsulated in carbon-nanotubes-grafted graphene sheets as advanced electrocatalysts for the hydrogen evolution reaction, *Adv. Mater.* 30 (2018) 1802011.

[46] L. Yan, H. Jiang, Y. Xing, Y. Wang, D. Liu, X. Gu, Nickel metal-organic framework implanted on graphene and incubated to be ultrasmall nickel phosphide nanocrystals as highly efficient water splitting electrocatalyst, *J. Mater. Chem. A* 6 (2018) 1682–1691.

[47] M. Zhang, Q. Dai, H. Zheng, M. Chen, L. Dai, Novel MOF-derived Co@N-C bifunctional catalysts for highly efficient Zn-air batteries and water splitting, *Adv. Mater.* 30 (2018) 1705431.

[48] Y. Li, B. Jia, Y. Fan, K. Zhu, G. Li, C.Y. Su, Bimetallic zeolitic imidazolate framework derived carbon nanotubes embedded with Co nanoparticles for efficient bifunctional oxygen electrocatalyst, *Adv. Energy Mater.* 7 (2017) 1702048.

[49] M. Kuang, Q. Wang, P. Han, G. Zheng, Cu, Co-embedded N-enriched mesoporous carbon for efficient oxygen reduction and hydrogen evolution reactions, *Adv. Energy Mater.* 7 (2017) 1700193.

[50] X.J. Zhao, P. Pachfule, S. Li, J.R.J. Simk, J. Schmidt, A. Thomas, Bifunctional electrocatalysts for overall water splitting from an iron/nickel-based bimetallic metal-organic framework/dicyandiamide composite, *Angew. Chem. Int. Ed.* 130 (2018) 9059–9064.

[51] D.H. Deng, K.S. Novoselov, Q. Fu, N.F. Zheng, Z.Q. Tiang, X.H. Bao, Catalysis with two-dimensional materials and their heterostructure, *Nat. Nanotech.* 11 (2016) 218–230.

[52] N. Mahmood, Y. Yao, J. Zhang, L. Pan, X. Zhang, J. Zou, Electrocatalysts for hydrogen evolution in alkaline electrolytes: mechanisms, challenges, and prospective solutions, *Adv. Sci.* 5 (2018) 1700464.

[53] G. Anandhababu, Y. Huang, D.D. Babu, M. Wu, Y. Wang, Oriented growth of ZIF-67 to derive 2D porous CoPO nanosheets for electrochemical-/photovoltage-driven overall-water-splitting, *Adv. Funct. Mater.* 28 (2018) 1706120.

[54] W. Xia, J. Li, T. Wang, L. Song, H. Guo, H. Gong, The synergistic effect of ceria and Co in N-doped leaf-like carbon nanosheets derived from a 2D MOF and their enhanced performance in the oxygen reduction reaction, *Chem. Commun.* 54 (2018) 1623–1626.

[55] K. Zhao, S. Liu, G. Ye, Q. Gan, Z. Zhou, Z. He, High-yield bottom-up synthesis of 2D metal-organic frameworks and their derived ultrathin carbon nanosheets for energy storage, *J. Mater. Chem. A* 6 (2018) 2166–2175.

[56] D.C. Marcano, D.V. Kosynkin, J.M. Berlin, A. Sinitskii, Z. Sun, A. Slesarev, L.B. Alemany, W. Lu, J.M. Tour, Improved synthesis of graphene oxide, *ACS Nano* 4 (2010) 4806–4814.

[57] F. Izumi, T. Ikeda, A Rietveld-analysis programm Rietan-98 and its applications to zeolites, *Mater. Sci. Forum* 198 (2000) 321–324.

[58] G. Kresse, J. Furthmüller, Efficiency of *ab-initio* total energy calculations for metals and semiconductors using a plane-wave basis set, *Comput. Mater. Sci.* 6 (1996) 15–20.

[59] P.E. Blochl, Projector augmented-wave method, *Phys. Rev. B* 50 (1994) 6671–6674.

[60] J.P. Perdew, J.A. Chevary, S.H. Vosko, K.A. Jackson, M.R. Pederson, D.J. Singh, C. Fiolhais, Atoms, molecules, solids, and surfaces: applications of the generalized gradient approximation for exchange and correlation, *Phys. Rev. B* 46 (1992) 6671–6674.

[61] J.P. Perdew, K. Burke, M. Ernzerhof, Generalized gradient approximation made simple, *Phys. Rev. Lett.* 77 (1996) 3865–3868.

[62] J. Deng, P.J. Ren, D.H. Deng, L. Yu, F. Yang, X.H. Bao, Highly active and durable non-precious-metal catalysts encapsulated in carbon nanotubes for hydrogen evolution reaction, *Energy Environ. Sci.* 7 (2014) 1919–1923.

[63] Y. Teng, H. Zhao, Z. Zhang, Z. Li, Q. Xia, Y. Zhang, MoS₂ nanosheets vertically grown on graphene sheets for lithium-ion battery anodes, *ACS Nano* 10 (2016) 8526–8535.

[64] G.H. Lee, M.C. Sung, J.C. Kim, H.J. Song, D.W. Kim, Synergistic effect of cugeo₃/graphene composites for efficient oxygen-electrode electrocatalysts in Li–O₂ batteries, *Adv. Energy Mater.* 8 (2018) 1801930.

[65] R.B. Wu, X.K. Qian, X.H. Rui, H. Liu, B. Yadian, K. Zhou, J. Wei, Q.Y. Yan, X.Q. Feng, Y. Long, L.Y. Wang, Y.Z. Huang, Zeolitic imidazolate framework 67-derived high symmetric porous Co₃O₄ hollow dodecahedra with highly enhanced lithium storage capability, *Small* 10 (2014) 1932–1938.

[66] R.B. Wu, X.K. Qian, K. Zhou, J. Wei, J. Lou, P.M. Ajayan, Porous spinel Zn_xCo_{3-x}O₄ hollow polyhedra templated for high-rate lithium-ion batteries, *ACS Nano* 8 (2014) 6297–6303.

[67] L.T. Yan, L. Cao, P.C. Dai, X. Gu, D.D. Liu, L.J. Li, Y. Wang, X.B. Zhao, Metal–Organic frameworks derived nanotube of nickel–cobalt bimetal phosphides as highly efficient electrocatalysts for overall water splitting, *Adv. Funct. Mater.* 27 (2017) 1703455.

[68] Z.L. Chen, R.B. Wu, M. Liu, H. Wang, H.B. Xu, Y.H. Guo, Y. Song, F. Fang, X.B. Yu, D.L. Sun, General synthesis of dual carbon-confined metal sulfides quantum dots toward high-performance anodes for sodium-ion batteries, *Adv. Funct. Mater.* 27 (2017) 1702046.

[69] Y. Zhu, L. Li, C. Zhang, G. Casillas, Z. Sun, A seamless three-dimensional carbon nanotube graphene hybrid material, *Nat. Commun.* 3 (2012) 1225–1131.

[70] D.W. Su, M. Cortie, G.X. Wang, Fabrication of N-doped graphene–carbon nanotube hybrids from Prussian blue for lithium–sulfur batteries, *Adv. Mater.* 7 (2017) 1602014.

[71] Z.F. Dai, H.B. Geng, J. Wang, Y.B. Luo, B. Li, Y. Zong, J. Yang, Y.Y. Guo, Y. Zheng, X. Wang, Q.Y. Yan, Hexagonal-phase cobalt monophosphosulfide for highly efficient overall water splitting, *ACS Nano* 11 (2017) 11031–11040.

[72] C. Tang, N.Y. Cheng, Z.H. Pu, W. Xing, X.P. Sun, NiSe nanowire film supported on nickel foam: an efficient and stable 3D bifunctional electrode for full water splitting, *Angew. Chem. Int. Ed.* 54 (2015) 9351–9355.

[73] H.Y. Jin, J. Wang, D.F. Su, Z.Z. Wei, Z.F. Pang, Y. Wang, In situ cobalt–cobalt oxide/n-doped carbon hybrids as superior bifunctional electrocatalysts for hydrogen and oxygen evolution, *J. Am. Chem. Soc.* 137 (2015) 2688–2694.

[74] H.Y. Li, S.M. Chen, X.F. Jia, B. Xu, H.F. Lin, H.Z. Yang, L. Song, X. Wang, Amorphous nickel–cobalt complexes hybridized with 1T-phase molybdenum disulfide via hydrazine-induced phase transformation for water splitting, *Nat. Commun.* 8 (2017) 15377–15387.

[75] J.J. Duan, S. Chen, C. Zhao, Ultrathin metal-organic framework array for efficient electrocatalytic water splitting, *Nat. Commun.* 8 (2017) 15341–15347.

[76] C. Wei, Z.J. Xu, The Comprehensive understanding of 10 mA cm⁻² as an evaluation parameter for electrochemical water splitting, *Small Methods* 2 (2018) 1800168.

[77] E.J. Popczun, C.G. Read, C.W. Roske, N.S. Lewis, R.E. Schaak, Highly active electrocatalysis of the hydrogen evolution reaction by cobalt phosphide nanoparticles, *Angew. Chem.* 126 (2014) 5531.

[78] C. Du, L. Yang, F.L. Yang, G.Z. Cheng, W. Luo, Nest-like NiCoP for highly efficient overall water splitting, *ACS Catal.* 7 (2017) 4131–4137.